



Monitoring volcano deformation at La Soufrière, St Vincent during the 2020–21 eruption with insights into its magma plumbing system architecture

Michal Camejo-Harry^{1,2*}, Karen Pascal^{2,3}, Pablo Euillades⁴,
Raphaël Grandin⁵, Ian Hamling⁶, Leonardo Euillades⁴,
Rodrigo Contreras-Arratia², Graham A. Ryan^{2,3}, Joan L. Latchman²,
Lloyd Lynch² and Minjeong Jo⁷

¹Department of Earth Sciences, University of Oxford, Oxford OX1 3AN, UK

²Seismic Research Centre, The University of the West Indies, St. Augustine, Trinidad and Tobago

³Montserrat Volcano Observatory, Flemmings, Montserrat, West Indies

⁴CEDIAC Institute, Universidad Nacional de Cuyo, Argentina

⁵Université de Paris, Institut de Physique du Globe de Paris, CNRS, F-75005 Paris, France

⁶GNS Science, New Zealand

⁷USRA, NASA-GSFC, Greenbelt, MD, USA

 MC-H, 0000-0001-5979-7497

*Correspondence: michal.camejo@earth.ox.ac.uk

Abstract: Measurements of surface deformation provide valuable insight into sub-volcanic processes operating before, during and after eruptions. Here, we investigate the drivers behind the 2020–21 effusive–explosive episode at La Soufrière volcano in St Vincent using Global Positioning System (GPS) and Interferometric Synthetic Aperture Radar (InSAR) data between 2018 and 2021, and geodetic modelling. We observe inflation up to six months before the start to the effusive phase, which continued as the dome extruded. Once the eruption transitioned to the explosive phase, the volcano rapidly deflated, the bulk happening within the first three days of explosions. Our analytical modelling distinguishes three pressure source depth ranges contributing to this eruptive episode: 16–20, c. 6 and <1 km. Deformation data are therefore in line with a vertically extensive magmatic system being tapped pre- and syn-eruption with interaction between deep and shallow reservoirs by ascending magma batches. The combined use of GPS and InSAR proved to be instrumental for constraining the deformation field active during this eruptive episode. The direction of future geodetic monitoring at La Soufrière should therefore utilize both techniques with a view towards maximizing coverage while making up for shortfalls in station upkeep and variations in satellite overpass regularity.

Supplementary material: Supporting quantitative information related to the geodetic observations and modelling used in this study are available at <https://doi.org/10.6084/m9.figshare.c.6477358>

La Soufrière, St Vincent is the most historically active subaerial volcano in the Lesser Antilles arc. Eruptions have been both explosive (1718, 1812, 1902–03, 1979) and effusive (1784, 1971–72), with the two most recent episodes exhibiting transitions between both styles. After 41 years of quiescence, La Soufrière re-awakened with an effusive (dome-forming) eruption on 27 December 2020. Dome growth continued until it was superseded by an explosive phase lasting from 9 to 22 April 2021. This fortuitous sequence of eruptive styles was instrumental in fast tracking the much-needed expansion of geodetic monitoring in St Vincent.

Geodetic data have been shown to be especially useful for detecting the accumulation of magma and volatiles as a harbinger to an eruption (Sparks *et al.* 2012) as well as assessing the geometry and volume of the active magma plumbing system (Fernandez *et al.* 2017; Magee *et al.* 2018). At La Soufrière, associated monitoring techniques began in the 1970s with the use of dry-tilt successfully recording the gradual inflation and rapid deflation preceding and following the 1979 explosive–effusive eruption (Fiske and Sigurdsson 1982; Fiske and Shepherd 1990). Global Positioning System (GPS) was introduced into routine geodetic monitoring in 2001,

From: Robertson, R. E. A., Joseph, E. P., Barclay, J. and Sparks, R. S. J. (eds) *The 2020–21 Eruption of La Soufrière Volcano, St Vincent*. Geological Society, London, Special Publications, **539**, <https://doi.org/10.1144/SP539-2022-270>

© 2023 The Author(s). This is an Open Access article distributed under the terms of the Creative Commons Attribution License (<http://creativecommons.org/licenses/by/4.0/>). Published by The Geological Society of London.

Publishing disclaimer: www.geolsoc.org.uk/pub_ethics

with short occupation campaigns using a network of benchmarks (eGPS), later supplemented by permanent continuously operating GPS (cGPS) installations in 2007 (Dondin *et al.* 2019). The addition of Interferometric Synthetic Aperture Radar (InSAR) as a complementary monitoring technique was initiated internally (Ryan *et al.* 2021) and progressed through external collaboration in response to the 2020–21 eruptive crisis. This was accompanied by a rapid densification of the cGPS network and reoccupation of eGPS benchmarks (Joseph *et al.* 2022).

At La Soufrière, human resource limitations prevented the real-time identification of precursory inflation from the then 2-station cGPS network. Infrequent eGPS occupations, a restricted pre-2021 cGPS network geometry, combined with a lack of volcanic activity since the start of GPS monitoring, have impeded attempts at characterizing the volcano's plumbing system architecture before now. Here, we describe the expansion of geodetic monitoring following the onset of the 2020–21 eruption of La Soufrière volcano. This includes the

deployment of additional GPS stations and the incorporation of InSAR datasets. We then retrospectively analyse available cGPS and InSAR (ALOS-2, SAOCOM-1 and Sentinel-1) time-series from 2018 for possible precursory deformation, and assess their individual effectiveness for geodetic monitoring in this region. Finally, we attempt to model the volcano's magma source architecture and integrate available seismic data to provide tighter constraints on eruptive processes.

Geodetic network expansion

Prior to the 2020–21 eruption, La Soufrière's ground deformation monitoring network consisted of two cGPS stations: SVGB and SVGK (Fig. 1), operated by The University of the West Indies Seismic Research Centre (UWI-SRC), headquartered in Trinidad. Data are transmitted via the internet using File Transfer Protocol (FTP) to UWI-SRC for processing and curation. On-island station maintenance is

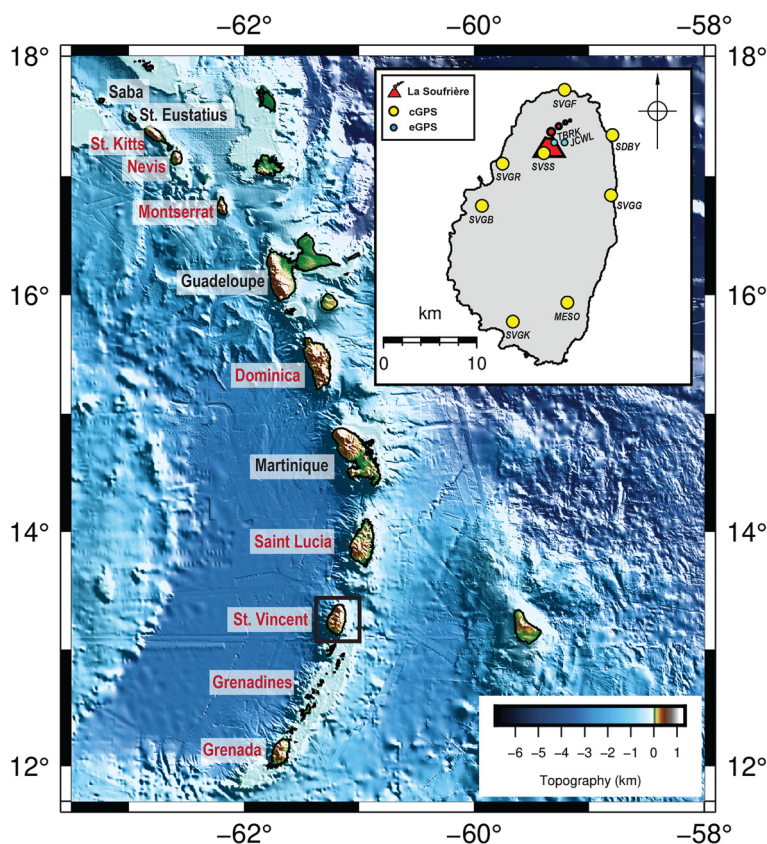


Fig. 1. Map of the Lesser Antilles arc. Territories monitored by UWI-SRC are labelled in red. Bathymetry is taken from GEBCO 2021. Inset map shows the GPS network operated on St Vincent during 2021.

Geodetic changes at 2020–21 La Soufrière eruption

carried out by the Soufriere Monitoring Unit (SMU). Until 2010, ‘regular’ (every few years) eGPS measurements were made by UWI-SRC scientists, with local support from the SMU. Financial constraints (high inter-island travel, operational and instrument costs) have since curtailed this practice and the growth of the cGPS network. In an attempt to address this deficit, UWI-SRC embarked on projects with GNS Science, New Zealand and JAXA (Japanese space agency) to investigate the effectiveness of InSAR for detecting volcanic deformation at the volcanic systems in its area of monitoring responsibility (Fig. 1) (Dondin *et al.* 2019). This technique had not yet been applied to St Vincent prior to the recent eruption.

GPS

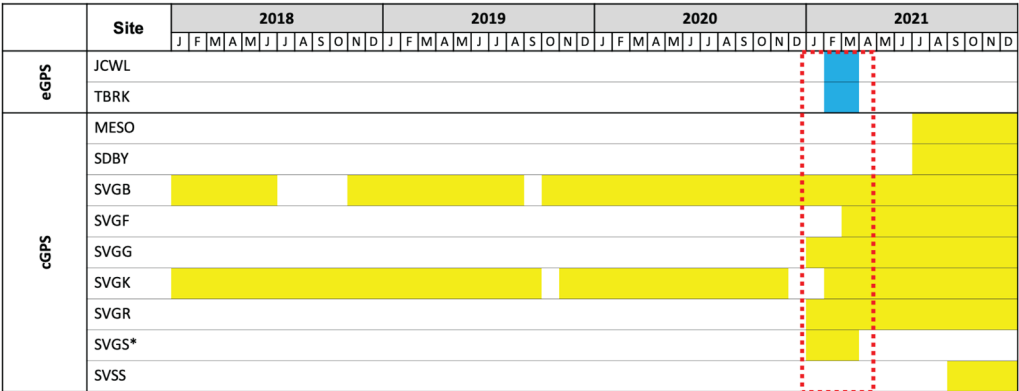
From inception, cGPS monitoring in St Vincent has been done using dual-frequency receivers (Table 1). Data are collected using a 30 s sampling interval for

a 24 h per UTC day. Instruments also record data at a higher sampling rate (1 s intervals); however, these are not routinely stored. Earliest installations SVGB (Belmont Observatory) and SVGK (Kingstown), located *c.* 9 and *c.* 19 km away from La Soufrière respectively (Fig. 1), have their antennas mounted on the roofs of buildings, using stainless-steel pins secured in cement.

The first indicator of precursory unrest related to this eruption was elevated seismicity in November 2020 (Joseph *et al.* 2022). Due to scientific contractual changes, this timing also coincided with the resumption of daily cGPS data processing alongside the backfilling of processing from earlier months. Furthermore, on 14 December 2020, SVGK functionality was lost and not restored until 16 February 2021 (Fig. 2). January 2021 saw the installation of three more cGPS stations in Georgetown (SVGG, *c.* 9 km away from the vent), volcano summit (SVGS, *c.* 1 km from the vent) and Richmond (SVGR, *c.* 5 km away from the vent), followed by

Table 1. Details of GPS sites deployed in St Vincent during the 2020–21 eruption

ID	Name	Location	Installation date	Equipment
JCWL	Jacob’s Well	13.3267° N, 61.1714° W	12 February 2021	Septentrio PolarRx5 receiver/ Trimble Zephyr 3 Geodetic antenna
TBRK	Table Rock	13.3278° N, 61.1783° W	20 February 2021	Septentrio PolarRx5 receiver/ Trimble Zephyr 3 Geodetic antenna
MESO	Mesopotamia	13.1781° N, 61.1672° W	21 July 2021	Septentrio PolarRx5 receiver/ Trimble Zephyr 3 Geodetic antenna
SDBY	Sandy Bay	13.3372° N, 61.1237° W	16 July 2021	Septentrio PolarRx5 receiver/ Trimble Zephyr 3 Geodetic antenna
SVGB	Belmont Observatory	13.2746° N, 61.2503° W	1 January 2007	Trimble NetR9 receiver/ Trimble Zephyr Geodetic antenna
SVGF	Fancy	13.3815° N, 61.1659° W	27 February 2021	Septentrio PolarRx5 receiver/ Trimble Zephyr Geodetic antenna
SVGG	Georgetown	13.2804° N, 61.1194° W	3 January 2021	Septentrio PolarRx5 receiver/ Trimble Zephyr Geodetic 2 antenna
SVGK	Kingstown	13.1622° N, 61.2284° W	24 December 2008	Trimble NetRS receiver/ Trimble Zephyr Geodetic antenna
SVGR	Richmond	13.3116° N, 61.2312° W	23 January 2021	Septentrio PolarRx5 receiver/ Trimble Zephyr 3 Geodetic antenna
SVGS	Volcano Summit (Destroyed during 9 April 2021 explosions)	13.3229° N, 61.1826° W	18 January 2021	Septentrio PolarRx5 receiver/ Trimble Zephyr Geodetic antenna
SVSS	Volcano Summit	13.3229° N, 61.1825° W	1 September 2021	Trimble NetRS receiver/ Trimble Zephyr 3 Geodetic antenna



*Destroyed during explosive phase

Fig. 2. Gantt chart showing the operational periods of GPS monitoring sites between 2018 and 2021. Bars are coloured by network type following Figure 1. The stippled, red polygon delineates the effusive start and explosive end to the eruption.

a fourth in Fancy (SVGF, *c.* 6 km away from the vent) in late February (Figs 1 & 2). SVGG and SVGR antennas were mounted on the roofs of buildings (e.g. Fig. 3b), while concrete monuments equipped with stainless steel threaded rods were constructed for SVGF and SVGS (Fig. 3c, d). The latter were built to substitute for solid bedrock which is absent in these locations, by manually digging pits

and constructing reinforced foundations connected to concrete pillars.

The expansion of the cGPS network from two to six stations dramatically improved its sensitivity. This was verified by estimations of variations in the minimum volume of an isotropic source (depth range 0–8 km) detectable by a 1 mm horizontal and 2 mm vertical displacement, which showed that the

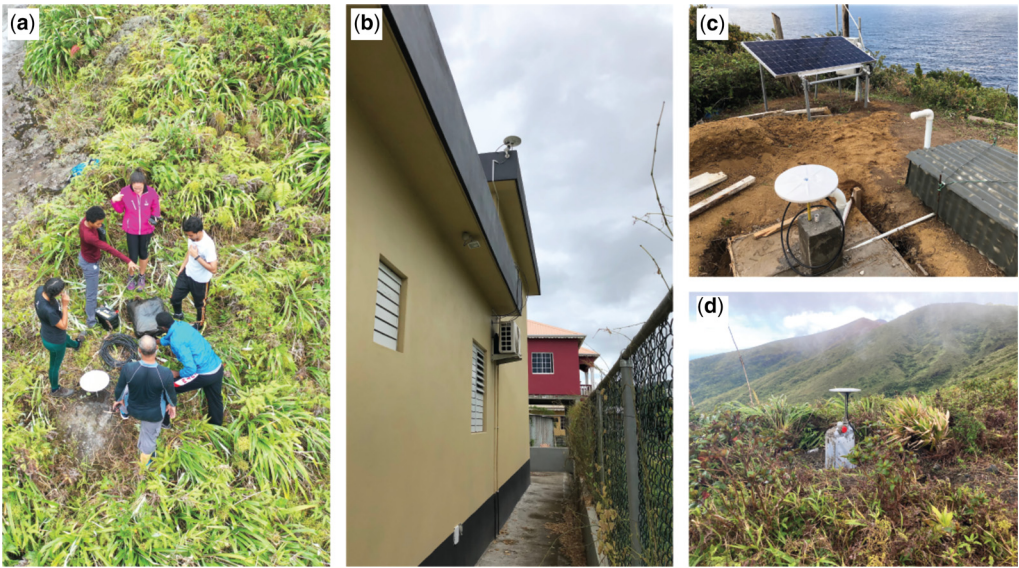


Fig. 3. Photographic examples of GPS monitoring sites. (a) eGPS setup at JCWL, February 2021. (b) cGPS rooftop antenna at SVGG, February 2021. (c) cGPS station at SVGF, February 2021. The GPS antenna is mounted on a reinforced concrete pillar built into a foundation. To the right is the collocated posthole seismometer. (d) cGPS station at SVGS, January 2021. The GPS antenna is mounted on a cement-filled pillar.

Geodetic changes at 2020–21 La Soufrière eruption

network had reasonably good geometry without major azimuthal gaps, but suffered from a lack of near-field stations to characterize shallow deformation sources (after [Beauducel *et al.* 2006](#)). Campaign-style GPS benchmarks were therefore reoccupied at two sites on the volcano's flanks (Jacob's Well, JCWL and Table Rock, TBRK, [Fig. 1](#)) during February and March of 2021 for at least 7 days at a time ([Figs 2 & 3a](#)). The antennas were mounted on stainless steel threaded rods drilled and cemented into pre-existing lava flows. It should be noted that these campaigns were conducted on foot whilst the dome continued to grow on the western edge of the pre-existing 1979 dome. This guided the choice of eGPS sites to the east, predicated upon life safety assessments and the westerly direction of the gas plume. The closest cGPS station to the volcano, SVGS, stopped working on 16 March and was subsequently destroyed during explosive eruptions in April ([Fig. 2](#)).

Following the end of the explosive phase to this eruptive episode, cGPS station deployment continued in 2021. In July, two stations were installed in Mesopotamia (MESO) and Sandy Bay (SDBY), and in September the summit station was replaced (renamed SVSS) in a slightly different location ([Figs 1 & 2](#)). Up to the time of writing, automatic data acquisition for MESO, SDBY and SVGF had not been achieved due to a lack of internet connection at those sites (communication to SVGF was lost during the explosive eruption). Data from these stations are downloaded approximately every fortnight by the SMU and sent to UWI-SRC via the internet for processing and storage. St Vincent's cGPS network now consists of 8 cGPS stations ([Fig. 1](#)), a sizeable improvement from its sparse pre-eruptive network.

InSAR

Despite the extensive spatial and temporal coverage expected from monitoring deformation fields using InSAR, this technique has not yet been incorporated into routine volcano monitoring by UWI-SRC. Contributing factors have ranged from budgetary to feasibility. Historically, there has been a lack of in-house specialist experience needed for interpreting satellite datasets. The application of InSAR to tropical volcanoes is also known to be inhibited by dense vegetation, large variations of water vapour and steep topography ([Ebmeier *et al.* 2013](#)), features which prevail in the Eastern Caribbean. Coherence is improved with increasing radar wavelengths, but the corollary of compounded limitations to freely available images is also true. Long satellite repeat-times (InSAR requires at least a pair of SAR images and preferably a longer time-series) are an added

hindrance towards real time InSAR measurements during unrest or eruptive episodes ([Ebmeier *et al.* 2018](#)).

The 2020–21 eruption crisis attracted an outpouring of support from the InSAR community in regional and international scientific organizations and research institutions: GNS Science (New Zealand), Institut de Physique du Globe de Paris (IPGP, France), National Aeronautics and Space Administration (NASA, USA), University of Leeds (UK), Universidad Nacional de Cuyo (Argentina) and United States Geological Survey (USGS, USA). This was a welcomed addition to UWI-SRC's geodetic monitoring efforts given the assertion that InSAR favours the detection of shallow (<5 km) deformation sources ([Ebmeier *et al.* 2018](#)). The first radar imagery used for observing eruption-related deformation was acquired from the open-source Sentinel-1 satellite (operating in C-band, $\lambda = 5.6$ cm), with interferograms provided by IPGP. Sentinel-1 repeat passes at that time occurred every 12 to 18 days. By contrast ALOS-2 imagery (operating in L-band, $\lambda = 23.5$ cm), originally made available under an ALOS-2 6th Research call project ([Ryan *et al.* 2021](#)) and subsequently through an emergency collaboration with NASA, had considerably longer repeat-times (approximately once per year) in the year building up to the eruption. UWI-SRC made formal requests to ESA (European Space Agency) and JAXA for additional satellite coverage that were subsequently granted, allowing Sentinel-1 to acquire images every six days and ALOS-2 every 14 days during the crisis. On the tail end of the crisis to support monitoring efforts, RCM (C-band, $\lambda = 5.6$ cm), COSMO-SkyMed (X-band, $\lambda = 3.1$ cm) and SAOCOM-1 (L-band, $\lambda = 23.5$ cm) interferograms were provided by USGS, University of Leeds and Universidad Nacional de Cuyo respectively, the latter of which only will be discussed here in detail.

Other techniques

Electronic Distance Measurements were conducted in February and March 2021 to monitor the stability of the SW crater wall, against which the dome was growing. No deformation was recorded during this period. The reader is directed to [Joseph *et al.* \(2022\)](#) for details of these measurements. Such exercises were discontinued just before the vulcanian explosions of April 2021.

Data processing

GPS

In preparation for processing, binary format receiver data collected from GPS sites are converted into

standard Receiver Independent Exchange (RINEX) format using the program TEQC (Estey and Meertens 1999). Raw receiver data and converted RINEX observation and navigation files are archived by UWI-SRC. Daily positions are calculated with GAMIT/GLOBK software (version 10.71) (Herring *et al.* 2018) using over 100 global (International Global Navigation Satellite Systems Service, IGS) reference stations with final orbits. To minimize tectonic influences, time-series of station positions are calculated relative to the ITRF2014 Caribbean Plate motion model as defined by Altamini *et al.* (2017).

InSAR

For this study, we processed Sentinel-1 (C-band) radar imagery acquired between 11 December 2017 and 30 April 2021 from descending track 156 and ascending track 164 (Table S1a, Fig. S1). During the eruptive crisis, continuous processing of Sentinel-1 interferograms acquired through effusive and explosive phases (27 December 2020–8 April 2021) was conducted by IPGP and shared with UWI-SRC. Processing techniques include the application of Small Baseline Technique (Doin *et al.* 2011), correction of atmospheric delays (Jolivet *et al.* 2011), adapted filtering and a tailored unwrapping strategy. Due to poor coherence outside the crater, detection of any deformation at the scale of the edifice was impossible with Sentinel-1, providing useful results only within the crater region. In other words, Sentinel-1 was essentially insensitive to any deep-seated signal (i.e. taking place at depth >2–3 km under the crater).

In order to provide constraints on deeper processes, we include images acquired by L-band satellites ALOS-2 and SAOCOM. Contrary to C-band, SAR data acquired in L-band have the capability of penetrating through vegetation, which gives access to deformation at the edifice scale, gaining resolution on processes taking place at greater depth. We processed ALOS-2 images between October 2014 and April 2021 (Table S1a) using GAMMA version 2.1 (Werner *et al.* 2000) and performed topographic corrections using the 30 m ASTER GDEM. Because of limited coherence in many of the interferograms due to long temporal baselines and dense vegetation across large parts of St Vincent, we used StaMPS (Hooper *et al.* 2007) to identify and extract stable scatterers to be used in forming an PS-SBAS time-series. In total we used 78 interferograms to form the time-series providing reasonable coverage around the edge of the island and summit area. Tropospheric delays were corrected assuming a linear correlation with elevation. In addition, we solved for and removed the best-fitting quadratic ramp from each interferogram.

We processed 12 SAOCOM ascending pass scenes acquired in stripmap mode S5 between 14 September 2019 and 14 March 2022 (Table S1a) applying software and methods used as for Roa *et al.* (2021), Boixart *et al.* (2020) and Velez *et al.* (2016). Due to a lack of coherence at the volcano edifice during the explosive phase, we did not compute a deformation time-series. We computed individual interferograms spanning the onset of the effusive phase centred at the crater and surroundings and co-eruptive interferograms spanning the explosive phase targeting the whole island. Topographic corrections were applied using the STRM 30 m DEM and interferograms were unwrapped using the MCF networks approach (Costantini 1998).

Geodetic observations

This section outlines the deformation signals detectable by both GPS and InSAR before (1 January 2018–26 December 2020), during (effusive phase: 27 December 2020–8 April 2021 and explosive phase: 9–22 April 2021) and after (23 April–31 December 2021) this eruption. We identify five distinct periods of deformation, each identified according to the technique used ('G' for GPS, 'I' for InSAR and 'GI' for GPS and InSAR).

G1: pre- and syn-eruptive (effusive) inflation far field

Pre-eruptive uplift can be observed on the then 2-station cGPS network from as early as July 2020 (Fig. 4). During the period 1 July to 9 December (between 10 December 2020 and 15 February 2021, SVGK was out of commission), sites expanded away from the volcano in an overall horizontal displacement of $5.8 (\pm 5.1)$ mm south and $6.9 (\pm 6.9)$ mm west for SVGB, and $7.3 (\pm 9.8)$ mm south and $3.7 (\pm 10.7)$ mm west for SVGK, with upward vertical motions $11.6 (\pm 6.0)$ mm for SVGB and $7.6 (\pm 15.8)$ for SVGK (Table 2). Inflation continued even as the volcano entered its effusive phase until late March 2021, which is clearly illustrated on SVGB's time-series (most apparent on the north–south component, Fig. 4a). SVGB's measured displacement over the period 1 July 2020 to 30 March 2021 was $13.7 (\pm 5.1)$ mm south, $7.1 (\pm 3.1)$ mm west and $10.4 (\pm 17.1)$ mm north (Table 2). Similar observations were not immediately obvious or ubiquitous across the rest of the cGPS network due to recording interruptions and new station installations. For example, the north–south component of SVGG showed an apparent southern trajectory from around February 2021 (Fig. 5c), while comparable movements were not observed on any other component or station.

Geodetic changes at 2020–21 La Soufrière eruption

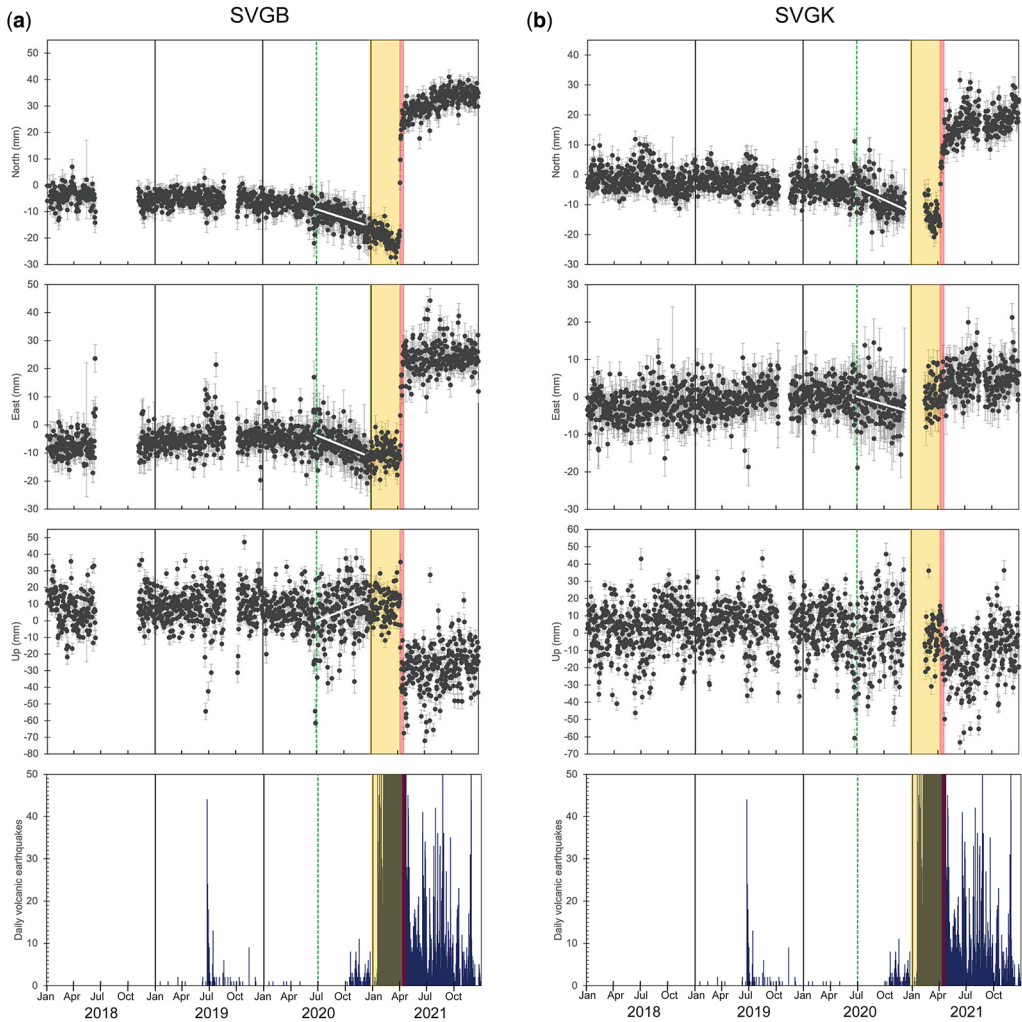


Fig. 4. Raw time-series of cGPS measurements for (a) SVGB and (b) SVGK stations from 2018 to 2021 (relative to the ITRF2014 Caribbean Plate motion model as defined by [Altamini et al. 2017](#)). Data are collected using a 30 s sampling interval for a 24 h per UTC day. Stippled green lines denote the observed start of pre-eruptive deformation. White lines illustrate the linear regression used to calculate displacements in [Table 2](#). Yellow and red bars correspond to effusive and explosive eruptive phases respectively. Included on the bottom panels are daily volcanic earthquake counts for the same period, as recorded by UWI-SRC. Volcanic earthquakes above 50 per day are not shown.

I2: near-field deformation

Near-field deformation was detected by Sentinel-1, ALOS-2 and SAOCOM and radar using images collected during 19–31 December 2020, January 2020–January 2021 and October 2020–February 2021 ([Table S1a & b](#)) respectively. The shorter frequency of Sentinel-1 acquisitions allowed for the detection of a deformation signal occurring between two consecutive acquisitions (both in ascending and descending passes), likely associated with the dome breaching the surface on 27 December 2020

([Joseph et al. 2022](#)). The deformation pattern is amplified within the crater and amounts to approximately 4 cm peak-to-peak displacement in the line-of-sight (LOS). The interferograms and preliminary models were communicated to UWI-SRC by IPGP on 11 January 2021, and are reported in [Joseph et al. \(2022\)](#).

Using ALOS-2 and SAOCOM data, negative LOS displacements of *c.* 80 mm were measured on the western edge of the crater consistent with uplift and/or westward motion ([Fig. 6](#)). Due to the timing of these acquisitions, both datasets contain the

Table 2. *Estimated displacements from cGPS time-series pre- and syn-eruption*

Site	dN (mm)	Propagated error (mm)	dE (mm)	Propagated error (mm)	dU (mm)	Propagated error (mm)
<i>1 July to 9 December 2020 (G1)</i>						
SVGB	−5.8	5.1	−6.9	6.9	11.6	6.0
SVGK	−7.3	9.8	−3.7	10.7	7.6	15.8
<i>1 July 2020 to 30 March 2021 (G1)</i>						
SVGB	−13.7	5.1	−7.1	3.1	10.4	17.1
<i>31 March to 8 April 2021 (G3)</i>						
SVGF	9.6	1.5	7.3	2.4	−3.7	4.3
<i>9–22 April 2021 (G4)</i>						
SVGB	42.5	2.8	37.1	3.5	−81.0	13.8
SVGF	−119.9	3.9	−41.0	4.3	−146.3	20.0
SVGG	67.9	2.5	−43.6	3.0	−65.1	12.6
SVGK	23.9	3.0	3.3	3.7	−27.3	15.1
SVGR	61.8	2.6	63.8	3.1	−97.5	13.0

dN, dE and dU denote estimated displacements for north, east and up components respectively. Offsets for G1 and G3 are estimated from a least-squares linear regression of time-series position data (shown in Figs 4 & 5). Propagated errors therefore consider residuals of the final and initial values of the linear regression. For G4, displacements are estimated using the *tsfit* program of GAMIT/GLOBK. Connectivity was lost to SVGF after 20 April 2021, therefore displacement for this station is calculated during 9–19 April.

displacement associated with the onset of the effusive eruption detected by Sentinel-1. The longer wavelength of ALOS-2 and SAOCOM radar facilitated higher coherence away from the dome exposing a slightly broader deformation signal than what was resolved using Sentinel-1 data. This points towards an additional shallow deformation source occurring sometime between October 2020 and January 2021 based on image acquisition dates.

G3: pre-explosive deformation

From 31 March to 8 April 2021, one of the closest operational cGPS stations to the volcano SVGF (Fig. 1) recorded small changes in deformation rates prior to the explosive phase (Fig. 5b). The most conclusive was observed on the horizontal components moving 9.5 (\pm 1.5) mm north and 7.3 (\pm 2.4) mm east.

G14: syn-eruptive (explosive) deflation

The start to the explosive phase of this eruption was accompanied by a rapid contraction of the entire cGPS network towards the volcano (Figs 4 & 5) consistent with depressurization of the magma reservoir. The overall horizontal and vertical station displacements measured during the explosive phase are shown in Table 2. The bulk of the deflation occurred within the first three days of explosions, coinciding with a drop in the daily volcanic earthquakes recorded from >300 per day just prior to 9 April to <124 per day between 9 and 12 April (Fig. 5). This deflation was also detected by SAOCOM

radar using interferograms covering the whole island (Fig. 7a, Table S1b). A LOS lengthening (subsidence) of up to 100 mm is observed affecting the western shore, whereas no significant LOS deformation is observed in the eastern shore due to the SAR slanted geometry. Inside the island, decorrelation did not allow us to characterize the whole deformation pattern, although deformation clearly increases towards the volcano. Such extensive deformation is not observed using images outside the explosive phase (Fig. S2). These results fit very well with the deformation time-series observed at different cGPS stations (Fig. S3) confirming that the SAOCOM signal is not an artefact of orbital uncertainties. Deformation then slowed down considerably during the remainder of the explosive phase.

G5: post eruption

Following the explosive phase, minimal deformation was observed, albeit modest northward movements in all stations suggestive of continued deflation (Figs 4 & 5). As the only station located north of the volcano, SVGF's movement steadily away from the volcano from May to August, before slowing down towards the end of 2021, deviates from this deflationary trend.

Modelling

To constrain the sources of deformation, we applied analytical models covering a range of source geometries where possible to three deformation periods

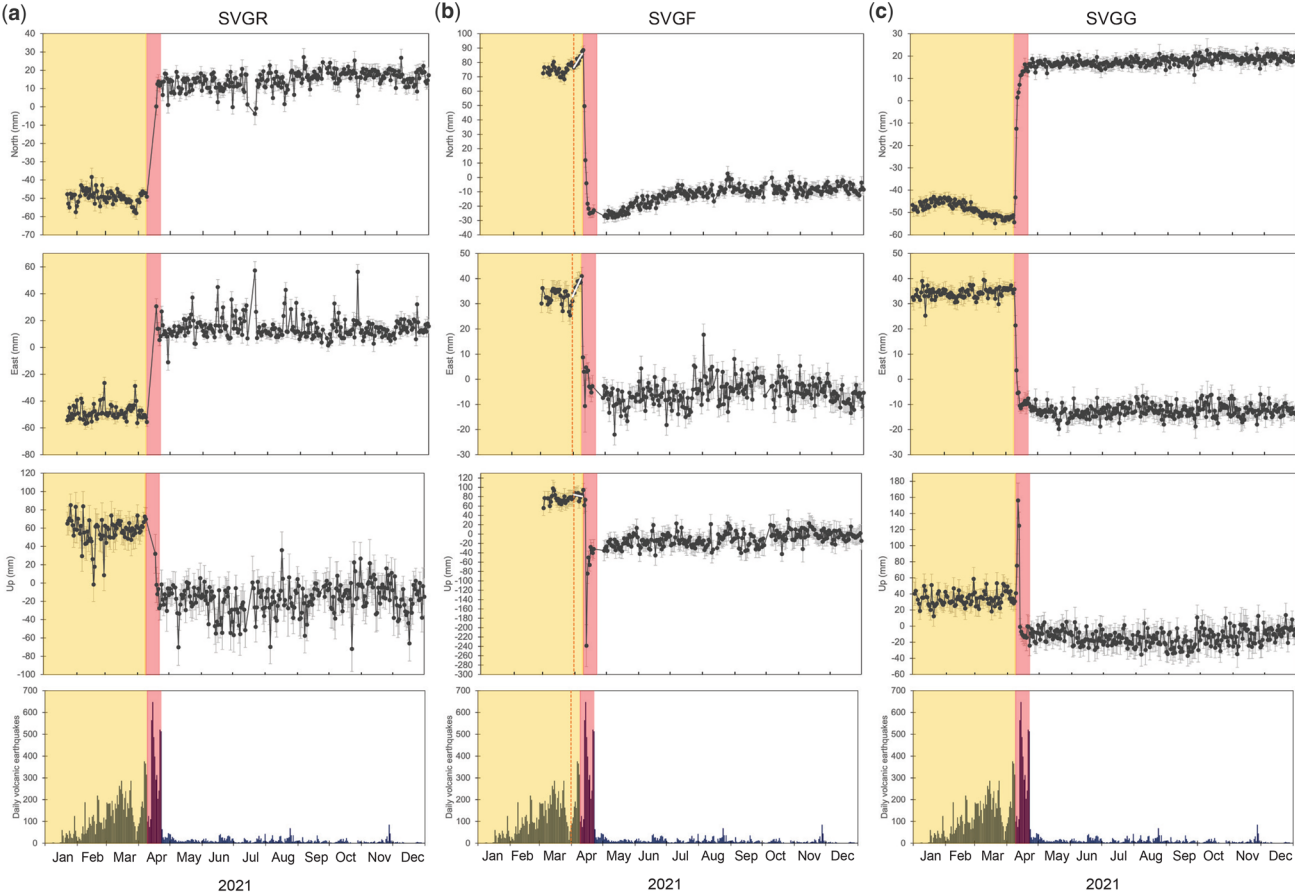


Fig. 5. Raw time-series of cGPS measurements for (a) SVGR, (b) SVGF and (c) SVGG stations for 2021 (relative to the ITRF2014 Caribbean Plate motion model as defined by Altamini *et al.* 2017). Data are collected using a 30 s sampling interval for a 24 h per UTC day. Yellow and red bars correspond to effusive and explosive eruptive phases respectively. Stippled orange lines on SVGF denotes possible deformation before start to explosive phase. White lines illustrate the linear regression used to calculate displacements in Table 2. The initial upward motion recorded by SVGG during the explosive phase is attributed to noise brought on by significant ash venting towards the east of the island. Included on the bottom panels are daily volcanic earthquake counts for the same period, as recorded by UWI-SRC. Note difference in y-axis scale compared to Figure 4.

M. Camejo-Harry *et al.*

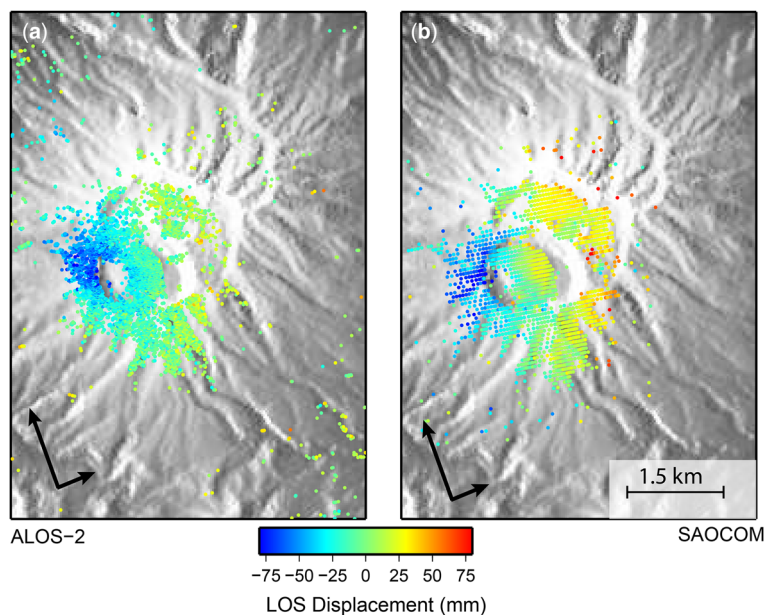


Fig. 6. Observed (a) ALOS-2 (15 January 2020–13 January 2021, ascending track, path 36, frame 250) and (b) SAOCOM (2 October 2020–23 February 2021, ascending track, path 29, frame 472) unwrapped interferograms illustrating near-field pre-eruptive (effusive) deformation. Negative LOS indicates motion towards the satellite.

(G1, I2 and GI4), assuming an isotropic, homogeneous elastic half-space, no topography and a Poisson’s ratio $\nu = 0.25$. Different modelling approaches are used each period, which will be detailed in each section.

Due to the fact that the models are conducted without accounting for topography, the estimated depths should be considered as relative to the average altitude of observations (*c.* 1 km above sea level). Periods G3 and G5 are excluded from analysis.

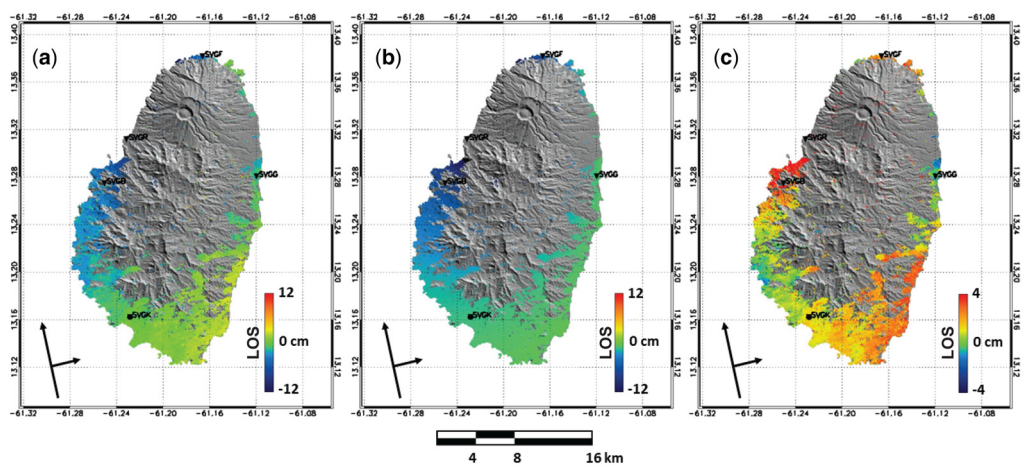


Fig. 7. (a) Observed, (b) modelled and (c) residual unwrapped interferograms for syn-eruptive (explosive) deformation phase using SAOCOM images obtained between 6 January 2021 and 14 March 2022 (ascending track, path 29 and frame 472). The forward model is computed using spherical source parameters (McTigue 1987) as derived from cGPS data (Table 4) only. Ground-based GPS stations are labelled. These data are not used in the inversion model for GI4 deformation as stated in the text.

Geodetic changes at 2020–21 La Soufrière eruption

G1: pre-eruptive inflation far field

We ran a set of [Mogi \(1958\)](#) forward models to approximate source parameters (depth and volume change) responsible for the precursory inflation over the 1 July to 9 December 2020 (period shortened from the start of the effusive phase since connectivity was lost to SVGK from 10 December, [Table 2](#), [Fig. 2](#)). Model input parameters include local source coordinates fixed to the vent (due to the restricted geometry of the 2-station cGPS network, both located west of the island and south of the vent ([Fig. 1](#))), depth range of 0–30 km and volume change 10^{-5} – 0.05 km^3 . We ran 100 000 forward models randomly sampling from the parameter space and assessing the RMS misfit for each model to the GPS observations. We found the best fit was at a depth of $18 (\pm 1.9) \text{ km}$ with a volume change of $29 (\pm 5) \times 10^6 \text{ m}^3$, providing a reasonable fit to the estimated displacement with an RMS misfit of 1.2 mm. The absence of detected deformation by Sentinel-1 in the same time interval (December 2017–December 2020) indicates that this deep source of deformation was not associated with a substantial counterpart at shallow depth.

I2: pre- and syn-eruptive (effusive) deformation near field

Modelling by [Joseph *et al.* \(2022\)](#) of Sentinel-1 acquisitions (19–31 December 2020) is compatible

with a shallow vertical dyke, starting at a depth of 0.7 km and reaching the surface along a 0.6 km long north–south-oriented crack, with a volume of $0.06 \times 10^6 \text{ m}^3$. This has been ascribed to syn-eruptive dome extrusion. The longer wavelength and time period (one year) covered by ALOS-2 radar provide an opportunity to investigate whether an additional deformation source can be unpicked from InSAR data pre-eruption. In this regard, we first remove the expected deformation caused by the shallow intrusion using a forward model and the dyke parameters detailed in [Joseph *et al.* \(2022\)](#) ([Fig. 8](#)). Due to the limited spatial extent of the InSAR data and high noise levels, rather than inverting for the deformation source directly we generate a suite of forward models to simulate the observed deformation testing three sources: point ([Mogi 1958](#)), dyke ([Okada 1985](#)) and penny-shaped crack (sill) ([Fialko *et al.* 2001](#)). We constrain the geometries using input parameters shown in [Table 3](#). As above, for each source we ran 100 000 forward models randomly sampling from the parameter space and assessing the RMS misfits for each model to the ALOS-2 observations ([Fig. S4](#)). To estimate the range of parameters, we extract the standard deviation of all models that provide a fit to the data within 10% of the best-fit solutions. For the dyke, the best-fit solution ([Fig. S5](#)) yields an RMS misfit of 11.7 mm with 54 modelled intrusions falling within 10%. The best-fitting dyke is c. 500 m long, dipping to the west at 69° with a thickness of c. 0.45 m ([Fig. 9](#)). The preferred models tend to favour

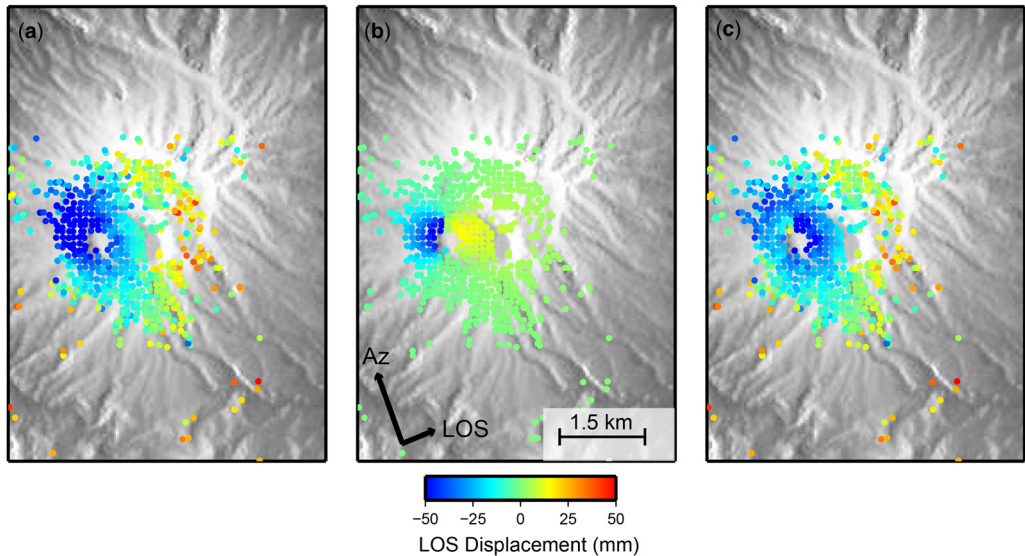


Fig. 8. Comparison of (a) ALOS-2 interferogram using images acquired between 15 January 2020 and 13 January 2021 (same as [Fig. 6a](#)), (b) predicted deformation from shallow dyke intrusion derived from Sentinel-1 data ([Joseph *et al.* 2022](#)) and (c) residual interferogram after removal of dyke intrusion.

Table 3. Modelling input parameters and results for pre-eruptive inflation near field (I2) using different sources

Dyke	Strike	Dip	Top depth (m)	Length (m)	Width (m)	Opening (m)	RMS (mm)
Input range	160°–200°	50–90° (both east and west dipping)	5–1000	500–3000	500–6000	0–1	11.7
Best fit	178° ± 9.8	69° west ± 11.3	648 ± 213	545 ± 463	1519 ± 463	0.5 ± 0.5	

Point (Mogi, 1958)	Location (east and north, m from origin)	Depth (m)	Volume change (km ³)	RMS (mm)	
Input range	1 km radius around vent	0–5000	1×10^{-5} – 0.05	13.0	
Best fit	103 ± 305, 312 ± 315	874 ± 289	$1.4 \times 10^{-4} \pm 9.9 \times 10^{-5}$		

Penny-shaped crack (Fialko <i>et al.</i> 2001)	Location (east and north, m from origin)	Depth (m)	Volume change (km ³)	Radius (m)	RMS (mm)
Input range	1 km radius around vent	0–5000	3×10^{-6} – 1.5×10^{-4}	100–2000	12.1
Best fit	–219 ± 114, 257 ± 140	1004 ± 276	$1.5 \times 10^{-4} \pm 4.6 \times 10^{-5}$	523.7 ± 157	

a westward dip (Fig. S4b) with opening values ranging from 0.05 to 1.7 m. The best-fitting point source (Fig. S5), which gives an RMS misfit of 12.1 mm, is located at a depth of *c.* 900 m around 200 m NE

of the vent with a volume increase of *c.* $0.1 \times 10^6 \text{ m}^3$ (Fig. 9). Of all the simulations, only 8 of the Mogi models provide fits to the data within 10% of the best solution clustering between *c.* 850

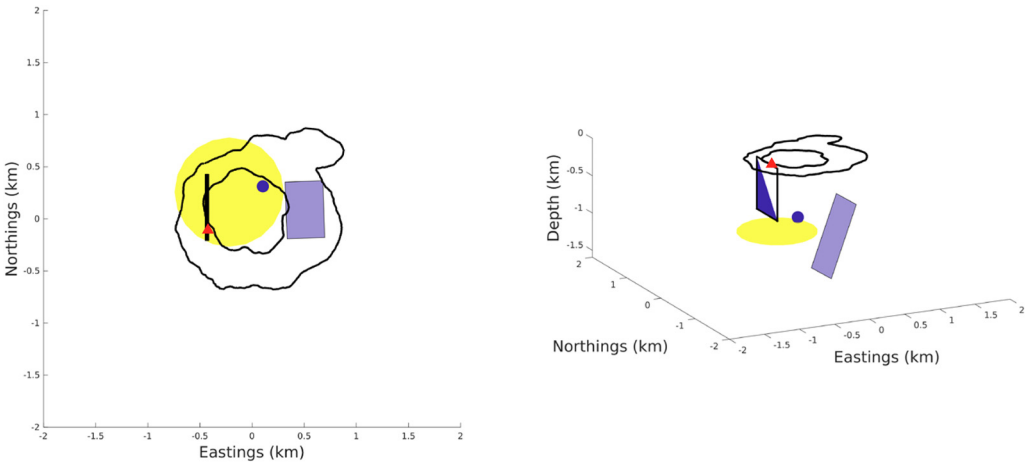


Fig. 9. Comparison of best-fit modelled sources for near-field pre-eruptive (effusive) deformation using ALOS-2 radar alongside source model for syn-eruptive (effusive) deformation using Sentinel-1 radar from Joseph *et al.* (2022). Black polygons denote the volcano crater (larger) and 1979 dome (smaller). Model sources are as follows: small blue circle = point source (Mogi 1958), purple rectangle = dyke and large yellow circle = penny-shaped crack (Fialko *et al.* 2001). The dyke modelled in Joseph *et al.* (2022) is denoted as a vertical rectangle half-filled in blue. The 2020 vent is shown as a red triangle.

Geodetic changes at 2020–21 La Soufrière eruption

Table 4. Results from Bayesian analysis (GBIS) for syn-eruptive (explosive phase, G4) deformation using different sources

Point (Mogi 1958)	X (m)	Y (m)	Depth (m)	$\Delta V \times 10^6 \text{ (m}^3\text{)}$						RMS (mm)
Optimal	773	2178	6052	50.2						26.5
2.5%	530	1824	5758	54.4						
97.5%	981	2500	6417	46.5						
Lower	−5000	−5000	1000	−100						
Upper	5000	5000	30 000	100						
Finite spherical (McTigue 1987)	X (m)	Y (m)	Depth (m)	Radius (m)	DP/μ					RMS (mm)
Optimal	776	2177	6059	25	−974					26.3
2.5%	539	1828	5747	12	−9219					
97.5%	982	2497	6398	59	−78					
Lower	−5000	−5000	100	5	−10 000					
Upper	5000	5000	30 000	5000	10 000					
Prolate ellipsoid (Yang <i>et al.</i> 1988)	X (m)	Y (m)	Depth (m)	Ax (m)	a/r	Strike	Plunge	DP/μ		RMS (mm)
Optimal	919	648	6045	6096	0.02	104	16	−0.22		37.7
2.5%	−162	712	4684	221	0.01	76	0.06	−136		
97.5%	915	2416	7422	5930	0.7	117	75	−0.06		
Lower	−5000	−5000	100	0	0.01	0.1	0	−10 000		
Upper	5000	5000	30 000	8000	1	359	90	10 000		
Horizontal rectangular sill (Okada 1985)	Length (m)	Width (m)	Depth (m)	Strike	X (m)	Y (m)	Opening (m)			RMS (mm)
Optimal	398	12 278	3	18	3298	4960	10			63.6
2.5%	137	2916	3	17	3164	4335	4.8			
97.5%	1088	14 684	79	23	4955	4996	10			
Lower	0	0	0	0	−5000	−5000	0			
Upper	15 000	15 000	30 000	360	5000	5000	10			

Note: Optimal is from the maximum *a posteriori* probability solution. The percentages 2.5% and 97.5% are the lower and upper boundaries of the 95% credible intervals. Lower and Upper are the bounds of the prior distribution used for the inversion. *X* and *Y* are the local coordinates of the source. Depth is positive downward. ΔV is the volume change. *Ax* is the length of the major semi-axis of the ellipsoid. *a/r* is the dimensionless aspect ratio between semi-axis (minor/major). Strike is the strike angle of the major semi-axis of the ellipsoid with respect to north in degrees. Plunge is the inclination angle of the major semi axis with respect to the horizontal in degrees. DP/μ is dimensionless excess pressure (pressure change/shear modulus). Opening is the opening of the dislocation plane. RMS (misfit between measured and modelled displacements) is calculated for both horizontal and vertical components; lowest values indicate the best model fit.

and 1700 m depth (Fig. S4a). For the sill, the best-fit model (Fig. S5) has an RMS misfit of 12.1 mm with a volume increase of $0.2 \times 10^6 \text{ m}^3$ at a depth of 1 km with a radius of *c.* 500 m (Fig. 9). All of the best-fitting models (51 total) lie between *c.* 450 m and *c.* 1.6 km focused beneath the vent area (Fig. S4c). InSAR points used in modelling are reported in Table S2a.

G14: syn-eruptive (explosive) deflation

The improved station density existing during the explosive phase allowed more source geometries to be tested. Here, using only GPS data, we apply a Bayesian approach implemented with open-source Geodetic Bayesian Inversion Software (GBIS) (Bagnardi and Hooper 2018), testing point (Mogi

1958), finite spherical (McTigue 1987), prolate ellipsoid (Yang *et al.* 1988) and horizontal rectangular sill (Okada 1985) models to our displacement data (Table 4). The inversion algorithm uses a Markov chain Monte Carlo method, incorporating the Metropolis–Hastings algorithm, to find posterior probability density functions of model parameters taking into account uncertainties in the data. Mogi (1958), McTigue (1987) and Yang *et al.* (1988) model sources all converged on land at various

locations NE of the vent, at depths of 6 km. Using RMS misfit (taking into account both horizontal and vertical displacements), the best fit was obtained using point and finite spherical source models (RMS misfit values 26.5 and 26.3 mm respectively). The prolate ellipsoid source had a higher RMS (37.7 mm), while a horizontal rectangular sill had the largest RMS misfit (63.6 mm), with the centre of the source located just off island to the north. We report on results obtained using

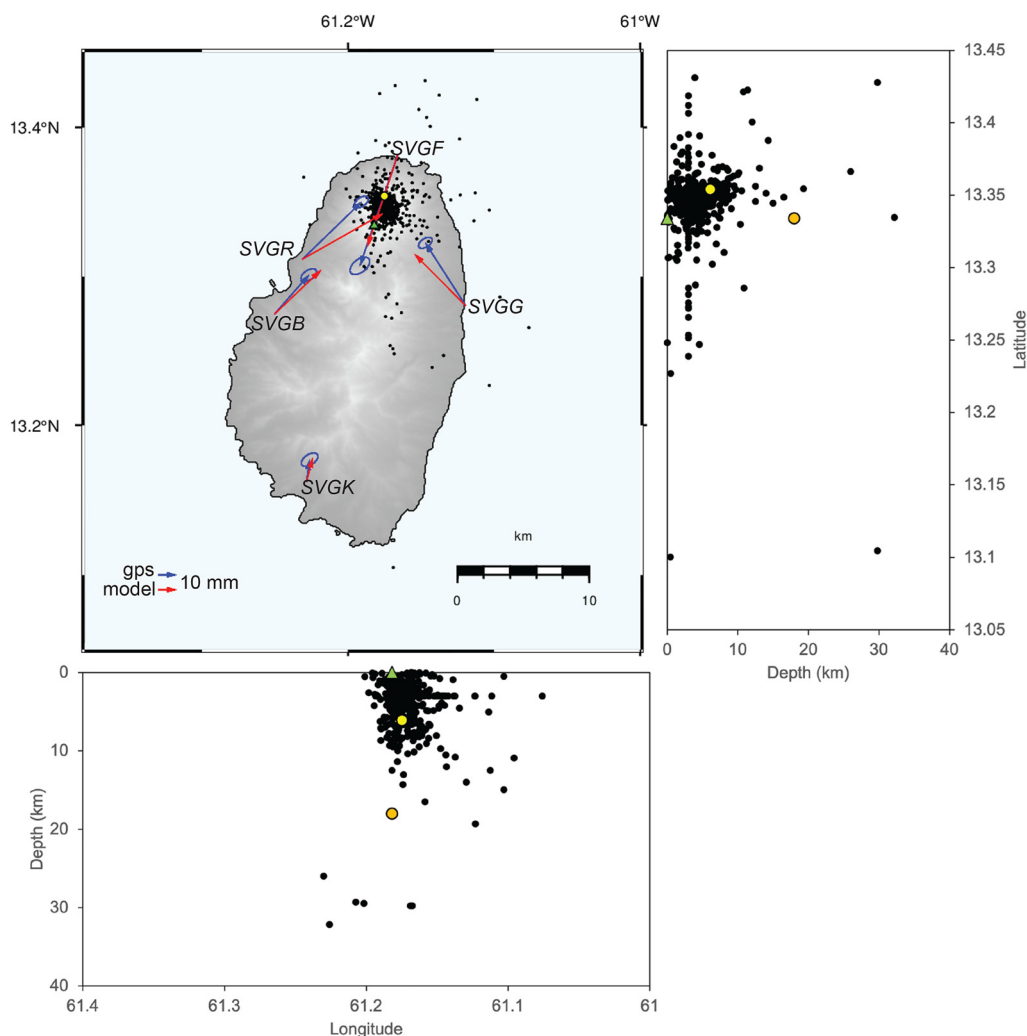


Fig. 10. Spatial relationship between syn-eruptive deflation (explosive phase 9–22 April 2021) as measured by the cGPS network, pre-explosive volcanic earthquakes (23 March to 6 April 2021) and modelled Mogi sources pre- and syn-eruption. The vent is shown as a green triangle. Observed horizontal displacement vectors, as measured by the cGPS network during 9–22 April 2021, are shown as blue arrows with associated uncertainties (95% confidence level) shown as blue ellipses. Modelled displacements (Mogi) are shown as red arrows. Mogi pre-eruptive (same location as vent) and syn-explosive sources are shown as orange and yellow spheres respectively. Earthquake epicentres (black circles) are taken from Joseph *et al.* (2022).

Geodetic changes at 2020–21 La Soufrière eruption

a simple Mogi point source (lowest number of changeable parameters), resolving at $6 (\pm 0.2)$ km depth with a volume change of $50 (\pm 2) \times 10^6 \text{ m}^3$ (Fig. 10).

Although an inversion was not attempted incorporating SAOCOM data, we computed a forward model (InSAR points used reported in Table S2b) with spherical source (McTigue 1987) parameters from Table 4 using dMODELS software package by Battaglia *et al.* (2013) confirming a close agreement with modelling results obtained using GPS data only (Fig. 7b, c).

Discussion

Analytical model limitations

We use analytical models to link the surface deformation recorded as ground displacements on St Vincent to La Soufrière's magma plumbing system, a feature we cannot directly observe from the surface. These models cover a range of geometries embedded in a homogeneous, isotropic and elastic half-space. The corollary is that this computational simplicity comes at the expense of their inherent assumptions, which do not capture the complexities of the natural situation (Taylor *et al.* 2021). Geophysical surveys have shown that isolated vats of liquid-dominated magma chambers with sharp transitions to surrounding country rock do not generally exist, with melts instead being disseminated via crystal mushes and closely spaced melt lenses (sills) over a wide depth range (Cashman *et al.* 2017). The mechanical behaviour of crystalline systems is distinct from melt and elastic host rock (Liao *et al.* 2018, 2021; Mullet and Segall 2022). Nonetheless, modelling magma reservoirs as dyke (Okada 1985), pressurized point (Mogi 1958) and finite spherical (McTigue 1987) sources provide the best fit to our data, and places some constraints on the depths of magma storage, associated volume changes and subsurface geometry. Prolate spherical (Yang *et al.* 1988) and horizontal sill (Okada 1985) source models are better able to simulate magma distribution over an extended depth range (e.g. Field *et al.* 2012). However, uncertainties introduced into ground-based and satellite data due to variations in station density and spatial coherence during unrest and eruptive periods, motivate us to focus here on results obtained using the simplest models with the lowest number of inversion parameters to provide first order insight into source depths and volumes. We acknowledge that there is usually a trade-off between source depth and volume when different source geometries are applied to deformation data (e.g. Pritchard and Simons 2004) and therefore expect the application of more sophisticated modelling techniques in the future to generate a larger range of acceptable results.

Relationship between modelled source volume change and erupted volume

Comparisons of geodetically modelled subsurface volume changes with eruptive volumes commonly show that the former are much smaller than the latter (McCormick Kilbride *et al.* 2016). This difference is controlled by competing influences of magma compressibility and magma reservoir properties including geometry and host rheology (Rivalta and Segall 2008; McCormick Kilbride *et al.* 2016; Wasser *et al.* 2021; Yip *et al.* 2022). Magma compressibility is fundamentally linked to gas exsolution within magma reservoirs. Volatiles dissolved in magma exsolve during decompression, cooling and crystallization, diminishing the pressure changes recorded by surface ground displacements. Relatedly, volatile-saturated magmas are ten times more compressible than magmas with no exsolved volatiles (Edmonds and Woods 2018). As alluded to in the previous section, although analytical models such as Mogi are widely used to estimate source parameters, they are highly idealized in simplifying the geometry and physical properties of the crustal magmatic system (Pascal *et al.* 2014; Taylor *et al.* 2021). As a result, modelling of a magma body within a perfectly elastic crustal rheology rather than a heterogeneous magma–mush network can lead to underestimations in the volume change of the magma reservoir and magma compressibility (Mullet and Segall 2022).

For the explosive phase (GI4), our modelled Mogi source volume change is $50 \times 10^6 \text{ m}^3 (\pm 2)$. This is near estimations by Cole *et al.* (2023) of erupted magma volume using mapped tephra deposits ($42 \times 10^6 \text{ m}^3 (\pm 20\%)$ Dense Rock Equivalent). Sparks *et al.* (2023) calculated the exploded volume up to 14 April 2021 using estimates of the duration of individual explosions from seismic observations and the magma flux from satellite observations of column height. Their results yield a comparatively higher volume of $83 \times 10^6 \text{ m}^3$, the majority of which emitted in the first three days, a time frame matching the bulk of measured syn-eruptive deflation (Figs 4 & 5). Interestingly the uncertainties surrounding this calculation (5th percentile $41 \times 10^6 \text{ m}^3$ and 95th percentile $142 \times 10^6 \text{ m}^3$) overlap with our volume. Depending on which estimate of erupted volume is used for comparison, our modelled reservoir volume change could be smaller or larger leading to contrasting inferences about magma compressibility.

Reconstructing the pre-eruptive exsolved volatile content of Soufrière magmas could place constraints on its compressibility prior to the explosive phase. However, a number of factors limit attempts at these estimations. For explosive eruptions, it can be assumed that total gas emissions are sourced entirely from the pre-eruptive exsolved volatile phase due to high magma ascent rates restricting

volatile exsolution between the chamber and the surface (Yip *et al.* 2022). Although total gas emissions were measured by satellites during La Soufrière's explosive phase (Joseph *et al.* 2022; Taylor *et al.* 2022), its effusive–explosive sequence complicates this association by introducing the probability for additional degassing within the conduit facilitated by slower extrusion rates. Unravelling these processes is further hampered by irregular gas measurements during the effusive phase, scrubbing by the hydrothermal system masking the actual volatile signature (Joseph *et al.* 2022) and lacking petrological determinations of volatile concentrations in melt inclusions or matrix glasses (Wasser *et al.* 2021).

Alternatively, we can use existing conceptual models to infer magma reservoir conditions pre-explosions. Stinton *et al.* (2023) posit that a shallow degassed magma plug left over from previous eruptions fed the effusive phase. This implies that low concentrations of pre-explosive exsolved volatiles were present in the magma reservoir with associated low magma compressibility. An incompressible magma scenario can also be reconciled with the continued inflation observed following the onset of dome extrusion. Segall (2016) shows that viscoelastic relaxation can manifest in inflation, rather than expected deflation post-eruption, for sufficiently incompressible magmas without the requirement for magma recharge.

Interpreting pre- and syn-eruptive deformation events within a structural framework

Notwithstanding its historical eruptive frequency, prior to the 2020–21 eruption, knowledge about the dynamics of La Soufrière's sub-volcanic system had been mainly constrained using petrological observations. It is thought to comprise a vertically extensive crystal mush network (melt contained in a framework of crystals) facilitating the differentiation of hydrous, mantle-derived high magnesium basalts over a range of depths spanning near the Moho to mid and upper crustal regions (Tollan *et al.* 2011; Melekhova *et al.* 2015). Preferred reservoirs for ascending magmas in various stages of evolution have been proposed by Fedele *et al.* (2021) to be *c.* 13 km, *c.* 7 km and *c.* 3.5 km. The products of eruptions over the last 1000 years have been predominantly homogeneous basaltic andesites (Cole *et al.* 2019) indicating a current steady-state regime; however, the drivers behind changes in eruptive style remain unclear. We attach geophysical observations to a developing petrological framework and infer the temporal evolution of the plumbing system during this eruption (Fig. 11).

Stage 1. Far-field precursory inflation was detected approximately 6 months in advance of this eruption, modelled at a source depth ranging 16–

20 km (including modelling uncertainty). This likely signalled the accumulation of basaltic andesite magmas and/or gas from depth. We cannot speculate as to the cause of this initiation. Petrological experiments place the generation of basaltic andesites beneath St Vincent in the lower crust (0.7–1 GPa) (Melekhova *et al.* 2015). Our modelled depth range is at the top of this pressure range.

Stage 2. From the timing of ALOS-2 and SAO-COM acquisitions, shallow precursory deformation occurred between October 2020 and January 2021. Based on our modelling, this signal can be explained either by (i) a shallow accumulation of magma at 800–1000 m depth or (ii) an eastward-propagating dyke to a top depth of *c.* 650 m. A pre-eruptive build of magma is supported by the Stinton *et al.* (2023) model whereby shallow degassed magma remnant from previous eruptions was remobilized and pushed out by gas-rich magma during the effusive phase. If this material was indeed the source of the 2021 dome extrusion, bulk rock chemical analyses support this assertion in being more silicic than 2021 explosive and 1979 material (Weber *et al.* 2023). Our alternative model, which has the best misfit to the data, suggests that there was a failed intrusion beneath the 1979 dome, likely representing a pre-existing pathway for magma extrusion. Arrested dykes are commonly observed (e.g. Gudmundsson 2011; Drymoni *et al.* 2020), with models suggesting that edifice heterogeneity as well as the local stress field are possible factors preventing an intrusion from reaching the surface (Dahm 2000; Gudmundsson 2011). Given the location of our best-fit dyke, we suggest that the pre-existing dome structure acted as a structural barrier causing the dyke to stall and fail to reach the surface. Priming of the shallow magma system by ascending basaltic andesite magmas and associated exsolved volatiles generated in Stage 1, followed by emplacement of the failed dyke are consistent with above-background seismicity recorded in November 2020 (Joseph *et al.* 2022).

Stage 3. The breaching of the dome through the surface in December 2020, west of the 1979 dome, was accompanied by shallow deformation modelled as a vertical dyke. This shift in the source location implies that magma found a more favourable path to the surface, perhaps unobstructed by the pre-existing 1979 dome. Once the effusive eruption began, the volcano continued to inflate at the scale of the edifice, seemingly uninterrupted whilst the dome extruded. This could be related to a continued influx of basaltic andesite magmas from depth with the extrusion of material at the surface being insufficiently vigorous to compensate for this overall pressure build-up. Alternatively, low compressibility of resident magma facilitated viscous creep of the surrounding host rock without new magma recharge from depth (Segall 2016).

Geodetic changes at 2020–21 La Soufrière eruption

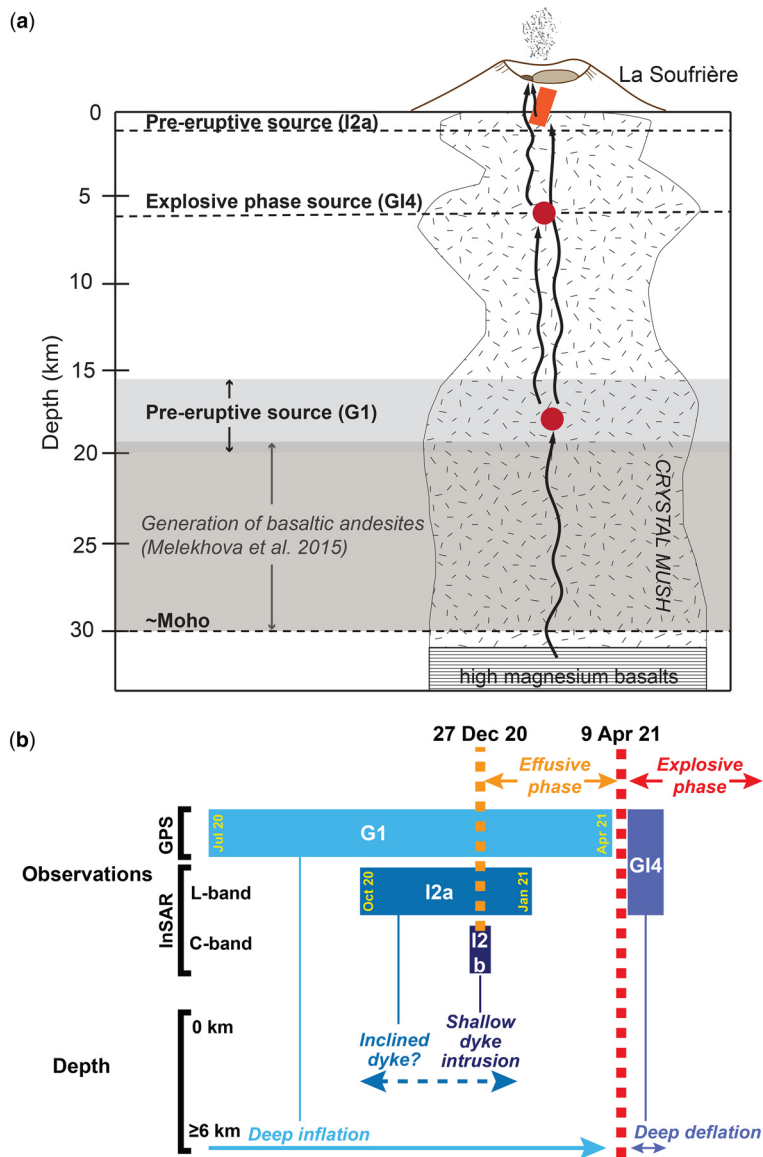


Fig. 11. (a) Schematic summary illustrating the vertically extensive and interconnected plumbing system architecture beneath La Soufrière as determined from geodetic observations. Basaltic andesite magmas, generated from mantle-derived high magnesium basalts, stall at preferred depths of 16–20 and c. 6 km (dark red spheres). Arrows show the inferred migration of magmas from different regions within the crust. At the surface, within the volcano crater, 2020 (left) and 1979 (right) domes are shown. The shallowest pressure source (<1 km) detected using InSAR likely represents the accumulation of magma from depth or remobilization of magma left over from previous eruptions prior to the 27 December 2020 effusive eruption. This is shown in orange to distinguish this region as partially to mostly crystalline (mushy) at these depths before the start of unrest. The best-fit source geometry is an eastward-propagating dyke likely representing a failed intrusion beneath the 1979 dome. (b) Pre- and syn-eruptive deformation stages detected using GPS and InSAR techniques, as described in the text. We distinguish the I2 phase detected via InSAR into a & b to highlight the detection pre- and syn-eruption deformation sources.

Stage 4. Prior to the explosive phase, an increased NE motion was observed on SVGF (c. 31 March 2021). However, this lone signal cannot be taken as an independent indicator of an augmented volcanic inflation rate. Nonetheless, this timing falls within the range of a number of key features

observed from other monitoring streams signalling a change in the dynamics of the magmatic system. Late March heralded the start of volcano-tectonic earthquake swarms (23–24 March), followed by their transition to greater depths from around 5 April (Fig. 10) (Joseph *et al.* 2022). Early April also saw an increase in dome volume and extrusion rate (Joseph *et al.* 2022). We hypothesize that in advance of the explosive phase, these changes could have been facilitated by an increase in magmatic overpressure favoured by a crater configuration where the dome effectively capped a significant portion of the crater floor, decreasing the efficiency of outgassing. Similar mechanisms related to edifice and conduit permeability have been proposed for changing eruptive styles at submarine Kick-em-Jenny volcano (Dondin *et al.* 2017). Alternatively or simultaneously, this period may represent the moment in which volatile-rich magmas reached the surface after all remnant degassed magma from previous eruptions was pushed out (Stinton *et al.* 2023).

Stage 5. Explosions began on 9 April 2021 accompanied by a deflation of the volcano. Our modelling places this pressure source at 6 km. This is marginally shallower than thermobarometric estimates of the magma reservoir feeding the current eruption from petrology (8–13 km depth) (Weber *et al.* 2023). Pre-explosive volcano-tectonic earthquakes span above and below our source depth (Fig. 10) likely emulating stress changes accompanying increasing overpressure and destabilization in the trans-crustal melt–mush system (e.g. Christopher *et al.* 2015) as the activity evolved from effusive to explosive. Seismic epicentres are offset from the vent mirroring the modelled explosive deflation source location (Fig. 10). Although detailed investigation into the mechanism behind pre-explosive seismicity at La Soufrière is beyond the scope of this paper, we postulate stress transfer to nearby fault structures (inferred on past geological maps e.g. Robertson 2005) relative to the conduit due to dyke inflation and/or elevated pore pressures in surrounding water-saturated aquifers known to be characteristic of La Soufrière's edifice (Lahr *et al.* 1994; White and Power 2001; Roman *et al.* 2008; Fournier *et al.* 2011).

SVGF's atypical behaviour

La Soufrière's northernmost cGPS station, SVGF (Fig. 1), was distinctive in increasing its horizontal motion just before the explosive phase and expanding away from the volcano after the 2020–21 eruption had ended (Fig. 5b). Here, we speculate as to the reasons for this curious behaviour. Out of all the stations deployed during the effusive phase, SVGF was the last to be completed (Fig. 2) and the

only monument-style installation (Fig. 3c) (SVGS is excluded from this since it went offline shortly after it was installed). It is therefore probable that data recorded by SVGF reflect the coinciding effects of concrete settling and magma withdrawal.

SVGF's time-series post-eruptive trajectory may also underscore some of La Soufrière's structural heterogeneities. Its edifice consists of an older stratocone or Somma, within which a younger pyroclastic cone emerges that has been the source of historical eruptions (Robertson 2005). Remnants of this Somma are defined by steep arcuate ridges north of the volcano comprising basaltic lava flows. Geographically, SVGF was the only station present during this eruption to reside upon this prehistoric edifice. Following the removal of pressure brought about by the explosive phase, it can be inferred that this distinct country rock surrounding the magma reservoir to the north influenced the partitioning of strain as the edifice rebounded inelastically during recovery (e.g. Head *et al.* 2019).

Utility of GPS and InSAR for volcano monitoring in the Caribbean: lessons from La Soufrière

The 2020–21 eruption propelled the integration of InSAR with traditional GPS monitoring at La Soufrière allowing for the effectiveness of each for detecting deformation to be equally assessed. During volcanic crises, monitoring scientists are largely interested in forecasting the start to and progression of eruptive activity for purposes of risk management. GPS was demonstrably the more successful technique for detecting precursory unrest in this scenario. Despite its sparsity, the lengthy time-series provided by the far-field 2-station cGPS network revealed deformation about 6 months before the effusive phase (G1), albeit not in real time. One of the major attractions of InSAR over GPS is the theoretically larger geographical extent the former captures, especially when compared to ground-based station networks. Yet, even with high return rates, the shorter wavelength of Sentinel-1 resulted in the coherent part of interferograms being restricted to the less vegetated crater area of the volcano. The longer wavelength instruments mounted on ALOS-2 and SAOCOM are capable of penetrating vegetation and generating interferograms that are coherent over a greater portion of the island. However, the very long repeat cycle of ALOS-2 and SAOCOM during the years prior to the eruption meant that the pre-eruptive pairs produced interferograms which were only coherent in the region of the volcanic crater and a little beyond it. Therefore InSAR was restricted to detecting near-field deformation before (and mostly throughout) the eruption, with only

Geodetic changes at 2020–21 La Soufrière eruption

ALOS-2 and SAOCOM radar uncovering pre-eruptive deformation using pre- and post-eruptive (effusive) pairs. Whilst providing additional, useful insight after the fact on shallow precursory deformation, the infrequency of ALOS-2 and SAOCOM acquisitions hypothetically thwarted the provision of this information during the unrest period.

After repeat times were increased for ALOS-2 in 2021, it was possible to generate interferograms that were coherent across much of the island. However, no obvious deformation related to continued dome growth was measured with this or SAOCOM radar. Although 2021 brought with it the densification of the GPS network, logistical challenges prevented the continuous operation of the summit station during the entire eruptive period, essentially restricting the network's detection capability to the far field. Deformation during the effusive phase was detected only by GPS. The closest station to the volcano (SVGF) detected a change in deformation rate days before the explosive phase. If this was indeed a definitive signal, the pressure source responsible for this change might have been characterized had the summit station (SVGS) been operational and/or satellite repeat times for longer wavelength radar (ALOS-2 and SAOCOM) been similar to this deformation timescale.

Once the explosions began, the extremely heavy ash fall and destruction of the crater area made it impossible to obtain coherent interferograms from post-explosive phase ALOS-2 (Fig. S6) and Sentinel-1 images. SAOCOM radar conversely was able to detect the syn-eruptive (explosive) deflation also measured by the cGPS network (Fig. 7). GPS instrumentation was also affected by ashfall with recording interruptions and the addition of noise to the data (Fig. 5).

Overall, our retrospective analysis of GPS and InSAR data reveals the wealth of information that could have been utilized before and during this eruption had they both been optimized/available in real time. GPS provided a more consistent data stream and is capable of detecting deformation sources covering a large depth range, but this is solely dependent on the density and functioning of the network. InSAR's applicability depended on the radar used, capable of detecting shallow (≤ 6 km) deformation sources when a cocktail of different satellites (preferably long wavelength) are used with frequent overpasses. For St Vincent, ideal InSAR monitoring would combine L-band (for improved coherence), high-spatial resolution (for detection of shallow processes), short revisit interval (to increase temporal resolution and mitigate atmospheric noise), and an open-access/near-real-time data dissemination strategy (to facilitate near-real-time exploitation in a crisis monitoring setting). At present, UWI-SRC's access to the required radar and associated processing

requirements is contingent upon collaboration. The forthcoming 2023 satellite mission NASA-ISRO SAR (NISAR) will offer an important opportunity for exploiting the application of InSAR to Lesser Antilles volcanoes with its L-band wavelength, 12-day repeat cycle and free data access policy. When both techniques are used together, resolution shortfalls in each can be compensated for, as demonstrated by this study.

Conclusions

We have used geodetic observations obtained from GPS and InSAR techniques gathered retrospectively and during the 2020–21 effusive–explosive eruption of La Soufrière volcano to approximate its magma plumbing system architecture down to the lower crust. The far-field cGPS network geometry (closest operational station 5 km from the vent) only allowed for a depth sensitivity to deformation events ≥ 6 km. Despite the various radar employed in this study (Sentinel-1, ALOS-2 and SAOCOM), InSAR was most useful for detecting shallower deformation events, otherwise imperceptible by the existing cGPS network. This was mainly due to limitations introduced by satellites with the highest penetrating wavelengths having infrequent overpasses. Together both techniques proved to be complementary resources for distinguishing the magmatic processes influencing this eruptive episode. Five deformation periods are identified: (1) deep and (2) shallow pre-eruptive inflation, (3) syn-eruptive (effusive) inflation, (4) syn-eruptive (explosive) deflation and (5) post-eruptive recovery. Our modelled source depth estimates support the growing concept of a vertically extensive magmatic system beneath La Soufrière with preferred magma storage regions at *c.* 16–20 km, *c.* 6 km and <1 km (Fig. 11). This broadly matches independent estimates from petrological studies on this volcano. However, although providing first-order constraints on magma reservoir depths, our analytical modelling approach does not fully characterize the geometry of the plumbing system. Such detail will require additional constraints provided by further petrological and geophysical studies, which will in turn allow geodetic modelling parameters to be better resolved. There is room for continued development of geodetic monitoring in St Vincent, including sustaining a consistent data stream from the current 8-station cGPS network and new station installations. This study highlights the benefits of integrating InSAR into routine monitoring at UWI-SRC for supplementing the GPS network especially in the near field where logistical challenges have historically impeded station upkeep.

Acknowledgements The authors are grateful to the Soufrière Monitoring Unit for field assistance during GPS

occupations, and the Japanese space agency (JAXA) and European Space Agency for tasking systematic ALOS-2 and Sentinel-1 acquisitions over La Soufrière during the eruptive period. We would like to thank S. Sparks, J. Blundy and W. Aspinall for valuable suggestions and discussion. Two anonymous reviewers provided helpful and constructive comments that improved the clarity of the paper.

Competing interests The authors declare that they have no known competing financial interests or personal relationships that could have appeared to influence the work reported in this paper.

Author contributions **MC-H:** conceptualization (lead), formal analysis (equal), investigation (equal), methodology (equal), software (equal), visualization (equal), writing – original draft (lead), writing – review & editing (lead); **KP:** conceptualization (supporting), formal analysis (equal), investigation (equal), methodology (equal), software (equal), writing – original draft (supporting), writing – review & editing (supporting); **PE:** conceptualization (supporting), formal analysis (equal), investigation (equal), methodology (equal), software (equal), visualization (equal), writing – original draft (supporting), writing – review & editing (supporting); **RG:** conceptualization (supporting), formal analysis (equal), investigation (equal), methodology (equal), software (equal), visualization (equal), writing – original draft (supporting), writing – review & editing (supporting); **IH:** conceptualization (supporting), formal analysis (equal), investigation (equal), methodology (equal), software (equal), visualization (equal), writing – original draft (supporting), writing – review & editing (supporting); **LE:** conceptualization (supporting), formal analysis (equal), investigation (supporting), methodology (equal), software (equal); **RC-A:** conceptualization (supporting), formal analysis (supporting), writing – review & editing (supporting); **GAR:** conceptualization (supporting), writing – review & editing (supporting); **JLL:** conceptualization (supporting), writing – review & editing (supporting); **LL:** conceptualization (supporting); **MJ:** conceptualization (supporting).

Funding information

MC-H acknowledges funding from a Royal Society Newton International Fellowship (NIF\R1\211276).

Data availability The data that support the findings of this study are available from The University of the West Indies Seismic Research Centre, Japanese Space Agency (JAXA) and Argentina Space Agency (CONAE) but restrictions apply to the availability of these data, which were used under licence for the current study, and so are not publicly available. Data are, however, available from the authors upon reasonable request and with permission of the above agencies.

References

Altamini, Z., Métivier, L., Rebischung, P., Rouby, H. and Collilieux, X. 2017. ITRF2014 plate motion model.

- Geophysical Journal International*, **209**, 1906–1912, <https://doi.org/10.1093/gji/ggx136>
- Bagnardi, M. and Hooper, A. 2018. Inversion of surface deformation data for rapid estimates of source parameters and uncertainties: a Bayesian approach. *Geochemistry, Geophysics, Geosystems*, **19**, 2194–2211, <https://doi.org/10.1029/2018GC007585>
- Battaglia, M., Cervelli, P.F. and Murray, J.R. 2013. dMO-DELS: a MATLAB software package for modeling crustal deformation near active faults and volcanic centers. *Journal of Volcanology and Geothermal Research*, **254**, 1–4, <https://doi.org/10.1016/j.jvolgeores.2012.12.018>
- Beauducel, F., Agung Nandaka, M., Cornet, F.H. and Diamant, M. 2006. Mechanical discontinuities monitoring at Merapi volcano using kinematic GPS. *Journal of Volcanology and Geothermal Research*, **150**, 300–312, <https://doi.org/10.1016/j.jvolgeores.2005.07.005>
- Boixart, G., Cruz, L.F., Cruz, R.M., Euillades, P.A., Euillades, L.D. and Battaglia, M. 2020. Source model for Sabancaya volcano constrained by DInSAR and GNSS surface deformation observation. *Remote Sensing*, **12**, <https://doi.org/10.3390/rs12111852>
- Cashman, K.V., Sparks, R.S.J. and Blundy, J.D. 2017. Vertically extensive and unstable magmatic systems: a unified view of igneous processes. *Science (New York, NY)*, **355**, <https://doi.org/10.1126/0.1126/science.aag3055>
- Christopher, T.E., Blundy, J. *et al.* 2015. Crustal-scale degassing due to magma system destabilization and magma-gas decoupling at Soufrière Hills Volcano, Montserrat. *Geochemistry, Geophysics, Geosystems*, **16**, 2797–2811, <https://doi.org/10.1002/2015GCO05791>
- Cole, P.D., Robertson, R.E.A., Fedele, L. and Scarpati, C. 2019. Explosive activity of the last 1000 years at La Soufrière, St Vincent, Lesser Antilles. *Journal of Volcanology and Geothermal Research*, **371**, <https://doi.org/10.1016/j.jvolgeores.2019.01.002>
- Cole, P.D., Barclay, J. *et al.* 2023. Explosive sequence of La Soufrière St Vincent April 2021: insights into drivers and consequences via eruptive products. *Geological Society, London, Special Publications*, **539**, <https://doi.org/10.1144/SP539-2022-292>
- Costantini, M. 1998. A novel phase unwrapping method based on network programming. *IEEE Transactions on Geoscience and Remote Sensing*, **36**, 813–821, <https://doi.org/10.1109/36.673674>
- Dahm, T. 2000. On the shape and velocity of fluid-filled fractures in the Earth. *Geophysical Journal International*, **142**, 181–192, <https://doi.org/10.1046/j.1365-246x.2000.00148.x>
- Doin, M.-P., Lodge, F. *et al.* 2011. Presentation of the small baseline NSBAS processing chain on a case example: the Etna deformation monitoring from 2003 to 2010 using Envisat data. *Proceedings of the Fringe 2011 Workshop*, 19–23 September, Frascati, Italy.
- Dondin, F.J.-Y., Heap, M.J., Robertson, R.E.A., Dorville, J.-F.M. and Carey, S. 2017. Flank instability assessment at Kick-'em-Jenny submarine volcano (Grenada, Lesser Antilles): a multidisciplinary approach using experiments and modeling. *Bulletin of Volcanology*, **79**, <https://doi.org/10.1007/s00445-016-1090-8>

Geodetic changes at 2020–21 La Soufrière eruption

- Dondin, F.J.-Y., Lynch, L. *et al.* 2019. The University of the West Indies-Seismic Research Centre Volcano Monitoring Network: Evolution since 1953 and Challenges in Maintaining a State-of-the-Art Network in a Small Island Economy. *Geosciences*, **9**, <https://doi.org/10.3390/geosciences9020071>
- Drymoni, K., Browning, J. and Gudmundsson, A. 2020. Dyke-arrest scenarios in extensional regimes: insights from field observations and numerical models, Santorini, Greece. *Journal of Volcanology and Geothermal Research*, **396**, <https://doi.org/10.1016/j.jvolgeores.2020.106854>
- Ebmeier, S.K., Biggs, J., Mather, T.A. and Amelung, F. 2013. Applicability of InSAR to tropical volcanoes: insights from Central America. *Geological Society, London, Special Publications*, **380**, 15–37, <https://doi.org/10.1144/SP380.2>
- Ebmeier, S.K., Andrews, B.J. *et al.* 2018. Synthesis of global satellite observations of magmatic and volcanic deformation: implications for volcano monitoring & the lateral extent of magmatic domains. *Journal of Applied Volcanology*, **7**, <https://doi.org/10.1186/s13617-018-0071-3>
- Edmonds, M. and Woods, A.W. 2018. Exsolved volatiles in magma reservoirs. *Journal of Volcanology and Geothermal Research*, **368**, 13–30, <https://doi.org/10.1016/j.jvolgeores.2018.10.018>
- Estey, L.H. and Meertens, C.M. 1999. TEQC: the Multi-Purpose Toolkit for GPS/GLONASS Data. *GPS Solutions*, **3**, 42–49, <https://doi.org/10.1007/PL00012778>
- Fedele, L., Cole, P.D., Scarpato, C. and Robertson, R.E.A. 2021. Petrological insights on the last 1000 years of explosive activity at La Soufrière volcano, St. Vincent (Lesser Antilles). *Lithos*, **392–393**, 106150, <https://doi.org/10.1016/j.lithos.2021.106150>
- Fernandez, J., Pepe, A., Poland, M.P. and Sigmundsson, F. 2017. Volcano Geodesy: recent developments and future challenges. *Journal of Volcanology and Geothermal Research*, **344**, 1–12, <https://doi.org/10.1016/j.jvolgeores.2017.08.006>
- Fialko, Y., Khazan, Y. and Simons, M. 2001. Deformation due to a pressurized horizontal circular crack in an elastic half-space, with applications to volcano geodesy. *Geophysical Journal International*, **146**, 181–190, <https://doi.org/10.1046/j.1365-246X.2001.00452.x>
- Field, L., Blundy, J., Brooker, R.A., Wright, T. and Yirgu, G. 2012. Magma storage conditions beneath Dabbahu Volcano (Ethiopia) constrained by petrology, seismicity and satellite geodesy. *Bulletin of Volcanology*, **74**, 981–1004, <https://doi.org/10.1007/s00445-012-0580-6>
- Fiske, R.S. and Shepherd, J.B. 1990. 12 Years of Ground-Tilt Measurements on the Soufrière of St. Vincent, 1977–1989. *Bulletin of Volcanology*, **52**, 227–241, <https://doi.org/10.1007/BF00334806>
- Fiske, R.S. and Sigurdsson, H. 1982. Soufrière Volcano, St. Vincent – observations of its 1979 Eruption from the Ground, Aircraft, and Satellites. *Science (New York, NY)*, **216**, 1105–1106, <https://doi.org/10.1126/science.216.4550.1105>
- Fournier, N., Moreau, M. and Robertson, R. 2011. Disappearance of a crater lake: implications for potential explosivity at Soufrière volcano, St Vincent, Lesser Antilles. *Bulletin of Volcanology*, **73**, 543–555, <https://doi.org/10.1007/s00445-010-0422-3>
- Gudmundsson, A. 2011. Deflection of dykes into sills at discontinuities and magma-chamber formation. *Tectonophysics*, **500**, 50–64, <https://doi.org/10.1016/j.tecto.2009.10.015>
- Head, M., Hickey, J., Gottsmann, J. and Fournier, N. 2019. The influence of viscoelastic crustal rheologies on volcanic ground deformation: insights from models of pressure and volume change. *Journal of Geophysical Research: Solid Earth*, **124**, 8127–8146, <https://doi.org/10.1029/2019JB017832>
- Herring, T.A., King, R.W., Floyd, M.A. and McClusky, S.C. 2018. *Introduction to GAMIT/GLOBK*. Massachusetts Institute of Technology, Cambridge, Massachusetts.
- Hooper, A., Segall, P. and Zebker, H. 2007. Persistent scatterer interferometric synthetic aperture radar for crustal deformation analysis, with application to Volcán Alcedo, Galápagos. *Journal of Geophysical Research: Solid Earth*, **112**, <https://doi.org/10.1029/2006JB004763>
- Jolivet, R., Gandin, R., Lasserre, C., Doin, M.-P. and Peltzer, G. 2011. Systematic InSAR tropospheric phase delay corrections from global meteorological reanalysis data. *Geophysical Research Letters*, **38**, <https://doi.org/10.1029/2011GL048757>
- Joseph, E.P., Camejo-Harry, M. *et al.* 2022. Responding to eruptive transitions during the 2020–2021 eruption of La Soufrière volcano, St. Vincent. *Nature Communications*, **13**, <https://doi.org/10.1038/s41467-022-31901-4>
- Lahr, J.C., Chouet, B.A., Stephens, C.D., Power, J.A. and Page, R.A. 1994. Earthquake classification, location, and error analysis in a volcanic environment: implications for the magmatic system of the 1989–1990 eruptions at redoubt volcano, Alaska. *Journal of Volcanology and Geothermal Research*, **62**, 137–151, [https://doi.org/10.1016/0377-0273\(94\)90031-0](https://doi.org/10.1016/0377-0273(94)90031-0)
- Liao, Y., Soule, S.A. and Jones, M. 2018. On the mechanical effects of poroelastic crystal mush in classical magma chamber models. *Journal of Geophysical Research: Solid Earth*, **123**, 9376–9406, <https://doi.org/10.1029/2018JB015985>
- Liao, Y., Soule, S.A., Jones, M. and Le Mevel, H. 2021. The mechanical response of a magma chamber with poroviscoelastic crystal mush. *Journal of Geophysical Research: Solid Earth*, **126**, <https://doi.org/10.1029/2020JB019395>
- Magee, C., Stevenson, C.T.E. *et al.* 2018. Magma plumbing systems: a geophysical perspective. *Journal of Petrology*, **59**, 1217–1251, <https://doi.org/10.1093/ptrology/egy064>
- McCormick Kilbride, B., Edmonds, M. and Biggs, J. 2016. Observing eruptions of gas-rich compressible magmas from space. *Nature Communications*, **7**, <https://doi.org/10.1038/ncomms13744>
- McTigue, D.F. 1987. Elastic stress and deformation near a finite spherical magma body: resolution of the point source paradox. *Journal of Geophysical Research: Solid Earth*, **92**, 12931–12940, <https://doi.org/10.1029/JB092iB12p12931>
- Melekchova, E., Blundy, J., Robertson, R. and Humphreys, M.C.S. 2015. Experimental evidence for polybaric differentiation of primitive arc basalt beneath St. Vincent,

- Lesser Antilles. *Journal of Petrology*, **56**, 161–192, <https://doi.org/10.1093/petrology/egu074>
- Mogi, K. 1958. Relations between the eruptions of various volcanoes and the deformations of the ground surfaces around them. *Bulletin of the Earthquake Research Institute*, **36**, 99–134.
- Mullet, B. and Segall, P. 2022. The surface deformation signature of a transcrustal, crystal mush-dominant magma system. *Journal of Geophysical Research: Solid Earth*, **127**, <https://doi.org/10.1029/2022JB024178>
- Okada, Y. 1985. Surface deformation due to shear and tensile faults in a half-space. *Bulletin of the Seismological Society of America*, **75**, 1135–1154, <https://doi.org/10.1785/BSSA0750041135>
- Pascal, K., Neuberg, J. and Eleonora, R. 2014. On precisely modelling surface deformation due to interacting magma chambers and dykes. *Geophysical Journal International*, **196**, 253–278, <https://doi.org/10.1093/gji/ggt343>
- Pritchard, M.E. and Simons, M. 2004. An InSAR-based survey of volcanic deformation in the central Andes. *Geochemistry, Geophysics, Geosystems*, **5**, <https://doi.org/10.1029/2003GC000610>
- Rivalta, E. and Segall, P. 2008. Magma compressibility and the missing source for some dike intrusions. *Geophysical Research Letters*, **35**, <https://doi.org/10.1029/2007GL032521>
- Roa, Y., Rosell, P., Solarte, A., Euillades, L., Carballo, F., García, S. and Euillades, P. 2021. First assessment of the interferometric capabilities of SAOCOM-1A: new results over the Domuyo Volcano, Neuquén Argentina. *Journal of South American Earth Sciences*, **106**, <https://doi.org/10.1016/j.jsames.2020.102882>
- Robertson, R. 2005. St. Vincent. In: Lindsay, J.M., Robertson, R.E.A., Shepherd, J.B. and Ali, S. (eds) *Volcanic Hazard Atlas of the Lesser Antilles*. Seismic Research Centre, The University of the West Indies, St. Augustine, Trinidad and Tobago, W.I., 241–261.
- Roman, D.C., De Angelis, S., Latchman, J.L. and White, R. 2008. Patterns of volcanotectonic seismicity and stress during the ongoing eruption of the Soufrière Hills Volcano, Montserrat (1995–2007). *Journal of Volcanology and Geothermal Research*, **173**, 230–244, <https://doi.org/10.1016/j.jvolgeores.2008.01.014>
- Ryan, G.A., Hamling, I.J., Pascal, K. and Camejo, M. 2021. *Monitoring Volcano-Deformation in the Eastern Caribbean Combining the Existing GPS Network and ALOS/ALOS-2 Data*. The University of the West Indies Seismic Research Centre.
- Segall, P. 2016. Repressurization following eruption from a magma chamber with a viscoelastic aureole. *Journal of Geophysical Research: Solid Earth*, **121**, 8501–8522, <https://doi.org/10.1002/2016JB013597>
- Sparks, R.S.J., Biggs, J. and Neuberg, J. 2012. Monitoring volcanoes. *Science (New York, NY)*, **335**, 1310–1311, <https://doi.org/10.1126/science.1219485>
- Sparks, S., Aspinall, W., Renfrew, I. and Stewart, R. 2023. Analysis of magma flux and eruption intensity during the explosive activity at the Soufrière de St Vincent, West Indies. *Geological Society, London, Special Publications*, **539**, <https://doi.org/10.1144/SP539-2022-286>
- Stinton, A., Sparks, R.S.J. and Huppert, H.E. 2023. Analysis of magma rheology from lava spreading and explosive activity during the 2020–2021 eruption of the Soufrière St Vincent with implications for eruption dynamics. *Geological Society, London, Special Publications*, **539**, <https://doi.org/10.1144/SP539-2022-284>
- Taylor, I.A., Grainger, R.G., Prata, A.T., Proud, S.R., Mather, T.A. and Pyle, D.M. 2022. Satellite measurements of plumes from the 2021 eruption of La Soufrière, St Vincent [Preprint]. *Atmospheric Chemistry and Physics Discussions*, in review, <https://doi.org/10.5194/acp-2022-772>
- Taylor, N.C., Johnson, J.H. and Herd, R.A. 2021. Making the most of the Mogi model: Size matters. *Journal of Volcanology and Geothermal Research*, **419**, <https://doi.org/10.1016/j.jvolgeores.2021.107380>
- Tollan, P.M.E., Bindeman, I. and Blundy, J.D. 2011. Cumulate xenoliths from St. Vincent, Lesser Antilles Island Arc: a window into upper crustal differentiation of mantle-derived basalts. *Contributions to Mineralogy and Petrology*, **163**, 189–208, <https://doi.org/10.1007/s00410-011-0665-9>
- Velez, M.L., Euillades, P., Blanco, M. and Euillades, L. 2016. Ground deformation between 2002 and 2013 from InSAR observations. In: Tassi, F. and Caselli, O. (eds) *Copahue Volcano. Active Volcanoes of the World*. Springer, https://doi.org/10.1007/978-3-662-48005-2_8
- Wasser, V.K., Lopez, T.M., Anderson, K.R., Izbekov, P.E. and Freymueller, J.T. 2021. Multidisciplinary constraints on magma compressibility, the pre-eruptive exsolved volatile fraction, and the H₂O/CO₂ molar ratio for the 2006 Augustine eruption, Alaska. *Geochemistry, Geophysics, Geosystems*, **22**, <https://doi.org/10.1029/2021GC009911>
- Weber, G., Blundy, J. *et al.* 2023. Petrology of the 2020–21 effusive to explosive eruption of La Soufrière volcano, St Vincent: insights into plumbing system architecture and magma assembly mechanism. *Geological Society, London, Special Publications*, **539**, <https://doi.org/10.1144/SP539-2022-177>
- Werner, C., Wegmüller, U., Strozzi, T. and Wisemann, A. 2000. Gamma SAR and interferometric processing software. *Proceedings of the ERS-ENVISAT Symposium*, 16–20 October, Gothenburg, Sweden.
- White, R.A. and Power, J.A. 2001. Distal volcano-tectonic earthquakes (DVT's): diagnosis and use in eruption forecasting. Paper presented at the AGU Fall Meeting, 10–14 December 2001, San Francisco.
- Yang, X.-M., Davis, P.M. and Dieterich, J.H. 1988. Deformation from inflation of a dipping finite prolate spheroid in an elastic half-space as a model for volcanic stressing. *Journal of Geophysical Research: Solid Earth*, **93**, <https://doi.org/10.1029/JB093iB05p04249>
- Yip, S.T.H., Biggs, J., Edmonds, M., Liggins, P. and Shorttle, O. 2022. Contrasting volcanic deformation in Arc and Ocean Island settings due to exsolution of magmatic water. *Geochemistry, Geophysics, Geosystems*, **23**, <https://doi.org/10.1029/2022GC010387>